The Astronomical Journal, 163:123 (11pp), 2022 March https://doi.org/10.3847/1538-3881/ac4960

OGLE-2014-BLG-0319: A Sub-Jupiter-mass Planetary Event Encountered Degeneracy with Different Mass Ratios and Lens-source Relative Proper Motions

Shota Miyazaki[1,19], Daisuke Suzuki[1,19], Andrzej Udalski[2,20], Naoki Koshimoto[3,4,19], David P. Bennett[3,4,19], Takahiro Sumi[1,19], Nicholas Rattenbury[5,19], Han Cheongho[6]
(Leading Authors),
Fumio Abe[7], Richard K. Barry[3], Aparna Bhattacharya[3,8], Ian A. Bond[9], Akihiko Fukui[10,11], Hirosane Fujii[1], Yuki Hirao[1], Stela Ishitani Silva[3,12], Yoshitaka Itow[7], Rintaro Kirikawa[1], Iona Kondo[1], Brandon Munford[5], Yutaka Matsubara[7], Sho Matsumoto[1], Yasushi Muraki[7], Arisa Okamura[1], Greg Olmschenk[3,13], Clément Ranc[14], Yuki K. Satoh[1], Taiga Toda[1], Paul J. Tristram[15], Hibiki Yama[1], Atsunori Yonehara[16]
(MOA Collaboration),
and
Radek Poleski[2], Przemek Mróz[17], Jan Skowron[2], Michal K. Szymański[2], Igor Soszyński[2], Pawel Pietrukowicz[2], Syzmon Kozłowski[2], Krzysztof Ulaczyk[2,18], and Łukasz Wyrzykowski[2]
(OGLE Collaboration)

[1] Department of Earth and Space Science, Graduate School of Science, Osaka University, 1-1 Machikaneyama, Toyonaka, Osaka 560-0043, Japan
[2] Astronomical Observatory, University of Warsaw, AI. Ujazdowskie 4, 00-478 Warszawa, Poland
[3] Code 667, NASA Goddard Space Flight Center, Greenbelt, MD 20771, USA
[4] Department of Astronomy, University of Maryland, College Park, MD 20742, USA
[5] Department of Physics, University of Auckland, Private Bag 92019, Auckland, New Zealand
[6] Department of Physics, Chungbuk National University, Cheongju 28644, Republic of Korea
[7] Institute for Space-Earth Environmental Research, Nagoya University, Nagoya 464-8601, Japan
[8] Department of Physics, University of Notre Dame, Notre Dame, IN 46556, USA
[9] Institute of Information and Mathematical Sciences, Massey University, Private Bag 102-904, North Shore Mail Centre, Auckland, New Zealand
[10] Department of Earth and Planetary Science, Graduate School of Science, The University of Tokyo, 7-3-1 Hongo, Bunkyo-ku, Tokyo 113-0033, Japan
[11] Instituto de Astrofísica de Canarias, Vía Láctea s/n, E-38205 La Laguna, Tenerife, Spain
[12] Department of Physics, The Catholic University of America, Washington, DC 20064, USA
[13] Universities Space Research Association, Columbia, MD 21046, USA
[14] Sorbonne Université, CNRS, UMR 7095, Institut d'Astrophysique de Paris, 98 bis bd Arago, F-75014 Paris, France
[15] University of Canterbury Mount John Observatory, P.O. Box 56, Lake Tekapo 8770, New Zealand
[16] Department of Physics, Faculty of Science, Kyoto Sangyo University, Kyoto 603-8555, Japan
[17] Division of Physics, Mathematics, and Astronomy, California institute of Technology, Pasadena, CA 91125, USA
[18] Department of Physics, University of Warwick, Gibbet Hill Road, Coventry, CV4 7AL, UK
Received 2021 October 25; revised 2021 December 17; accepted 2021 December 27; published 2022 February 10

Abstract

We report the discovery of a sub-Jovian-mass planet, OGLE-2014-BLG-0319Lb. The characteristics of this planet will be added into a future extended statistical analysis of the Microlensing Observations in Astrophysics (MOA) collaboration. The planetary anomaly of the light curve is characterized by MOA and OGLE survey observations and results in three degenerate models with different planetary-mass ratios of $q = (10.3, 6.6, 4.5) \times 10^{-4}$. We find that the last two models require unreasonably small lens-source relative proper motions of $\mu_{\rm rel} \sim 1$ mas yr^{-1}. Considering Galactic prior probabilities, we rule out these two models from the final result. We conduct a Bayesian analysis to estimate physical properties of the lens system using a Galactic model and find that the lens system is composed of a $0.49^{+0.35}_{-0.27}$ $M_{\rm Jup}$ sub-Jovian planet orbiting a $0.47^{+0.33}_{-0.25}$ $M_{\odot}$ M dwarf near the Galactic Bulge. This analysis demonstrates that Galactic priors are useful to resolve this type of model degeneracy. This is important for estimating the mass-ratio function statistically. However, this method would be unlikely successful in shorter timescale events, which are mostly due to low-mass objects, like brown dwarfs or free-floating planets. Therefore, careful treatment is needed for estimating the mass-ratio function of the companions around such low-mass hosts, which only the microlensing can probe.

Unified Astronomy Thesaurus concepts: Gravitational microlensing (672); Binary lens microlensing (2136); Exoplanet astronomy (486); Exoplanet detection methods (489); Exoplanets (498)

1. Introduction

To date, more than 4000 exoplanets have been discovered (Akeson et al. 2013), revealing the universality and the diversity of planetary systems. Most of the known planets were discovered by the transit (Charbonneau et al. 2000) and the radial-velocity (RV; Butler et al. 2006) methods that are relatively sensitive to planets massive and close to their host stars, and thus the distribution of close-orbit exoplanets within ∼1 au have been

[19] MOA collaboration.
[20] OGLE collaboration.

revealed in detail by these methods (e.g., Marcy et al. 2005; Cumming et al. 2008; Howard et al. 2012; Fressin et al. 2013). By contrast, gravitational microlensing has a unique sensitivity to wide-orbit planets down to an Earth mass (Gould & Loeb 1992; Bennett & Rhie 1996) beyond the snow line where planet formation is considered to be the most efficient in the core accretion model (Lissauer 1993). This sensitivity is complementary to that of other detection methods.

The most recent statistical analysis using the largest sample of microlensing planets was conducted by Suzuki et al. (2016), who studied six years of survey data from the second phase of the Microlensing Observations in Astrophysics (MOA-II; Bond et al. 2001; Sumi et al. 2003) collaboration, including 23 planets discovered from 1474 microlensing events in 2007–2012. They find that the planet-frequency function in the power law describing planet/host mass ratio q has a break around $q \sim 2 \times 10^{-4}$, which implies Neptune-mass-ratio planets are the most abundant type of planet beyond the snow line. Moreover, Suzuki et al. (2018) compared the mass-ratio function with planet population synthesis models (Ida & Lin 2004) and found a discrepancy over the range $10^{-3} < q < 4 \times 10^{-3}$ of a factor of ∼10, suggesting there is no desert of sub-Saturn-mass planets beyond the snow line. This is contrary to the prediction from the runaway accretion process in the core accretion model (e.g., Pollack et al. 1996). This result is also recently confirmed by the CORALIE/HARPS sample of planets found by the RV method (Bennett et al. 2021). These comparisons between observations and theories can provide opportunities to quantitatively diagnose sources of problems in calculation or theory (Suzuki et al. 2018). The MOA collaboration is planning to present new results of a statistical analysis using the extended sample of Suzuki et al. (2016) including ∼50 planets detected by the MOA-II survey (D. Suzuki et al. 2022, in preparation). OGLE-2014-BLG-0319Lb, which is detailed in this paper, will be entered into this statistical sample.

In general, planetary signals in microlensing events appear as short-lived anomalous deviations from typical single-lens light curves (Paczynski 1986; Mao & Paczynski 1991) and sometimes produce a degeneracy problem where several model interpretations are possible for an anomaly. The origins of the degeneracy in microlensing events are summarized in detail in Han et al. (2018). Identifying all possible models and degeneracies for each planetary event is important for the completeness of a statistical microlensing analysis because a systematic analysis with automated parameter searches can sometimes miss the best-fit models for each event (e.g., OGLE-2013-BLG-0911; Shvartzvald et al. 2016; Miyazaki et al. 2020). Furthermore, investigating the origin of the degeneracy for each event is important because this adds to the growing body of literature on this topic and thus helps avoid missing models in future analyses.

In this paper, we analyze a microlensing event OGLE-2014-BLG-0319 that presents three planetary interpretations of different mass ratios of $q = (10.3,\ 6.6,\ 4.5) \times 10^{-4}$ and investigate the origin of the model degeneracy. The structure of this paper is as follows. In Section 2, we describe the observation and the data sets of the event. We present our light-curve analysis and discuss the degeneracy in Section 3. We estimate physical properties of the lens and source systems in Section 4 and finally summarize and discuss the result in Section 5.

2. Observations and Data Reductions

The microlensing event OGLE-2014-BLG-0319 occurred at $(\alpha,\ \delta)_{\rm J2000} = (17{:}47{:}50.68,\ -33{:}56{:}06.16)$, which corresponds to $(l,\ b) = (-4.0306,\ -2.9971)$ in Galactic coordinates. The fourth phase of the Optical Gravitational Lensing Experiment (OGLE-IV; Udalski et al. 2015) collaboration first discovered and reported the event on 2014 March 21 (about 50 days before the peak) through their Early Warning System (Udalski 2003). The OGLE field (BLG603) in which the event occurred was observed at a cadence of once per night by their 1.3 m Warsaw telescope at Las Campanas Observatory in Chile using the OGLE-IV camera that has a 1.4 deg^2 field of view (FOV). OGLE uses the standard Kron−Cousins I-band filter in their regular surveys. They also use the V-band filter in their occasional observations in order to mainly measure source star color. For this event, they did not conduct any V-band observations.

Independently, the second phase of the Microlensing Observations in Astrophysics (MOA-II) collaboration identified and reported the event as MOA-2014-BLG-171. The MOA field (gb1) in which the event occurred was observed at a cadence of once per 45 minutes by their 1.8 m MOA-II telescope at Mount John Observatory in New Zealand using the MOA-cam3 camera, which has a 2.2 deg^2 FOV (Sako et al. 2008). MOA uses in their regular survey observations a custom bandpass filter, named MOA-Red, which is similar to the sum of the standard Kron−Cousins I- and R-band filters. They also occasionally conduct V-band observations, but they did not observe in the V-band when the source star was magnified.

The data reductions for the OGLE and MOA data were conducted using their photometry pipelines (Wozniak 2000; Bond et al. 2001), which are optimized in their implementations of the different image analysis (DIA; Alard & Lupton 1998) method. The OGLE photometry is calibrated to the standard Cousins I band (Szymański et al. 2011). In the MOA data, we found significant systematic variations in the light curve that are likely to be correlated with the seeing and airmass values. We measured and corrected the systematic trends by running a detrending code (Bond et al. 2017), which yielded a χ^2 improvement of $\Delta\chi^2 \sim 0.3$ per data point in the baseline and thus significantly reduced the systematic trends in the MOA light curve. We ran several of our detrending codes as used in Koshimoto et al. (2017) and confirmed that these corrections are consistent with each other. We also confirmed that this detrending procedure hardly affects the best-fit parameters for this event.

In general, for crowded stellar regions toward the Galactic Bulge, the error bars derived by each photometry pipeline are underestimated (or overestimated), which can lead to incorrect conclusions and uncertainties for physical parameters. In order to correct this, we renormalize the error bars by $\sigma_i' = k\sqrt{\sigma_i^2 + e_{\rm min}^2}$, where σ_i and σ_i' are the original and corrected error bars in magnitude, respectively, and k and $e_{\rm min}$ are renormalization coefficients (Bennett et al. 2008; Yee et al. 2012). We select k and $e_{\rm min}$ to satisfy $\chi^2/{\rm dof} = 1$ for each data set (where dof is the number of degrees of freedom) and ensure that the cumulative χ^2 distribution sorted by the source magnification is as uniform a cumulative distribution as possible. We first find a preliminary best-fit model using the original light curves. Next, we renormalize the error bars by applying k and $e_{\rm min}$ values to satisfy the conditions referred above. Finally, we find the final best-fit model fitting all of the renormalized light curves. We note

Table 1
Data Sets for OGLE-2014-BLG-0319

Label	Telescope	Passband	$N_{\rm data}$[a]	k[b]	$e_{\rm min}$[b]
MOA	MOA-II 1.8 m	MOA-Red	3147	1.891	0.003
OGLE	Warsaw 1.3 m	I	724	1.306	0.013

Notes.
[a] The number of the data points.
[b] The coefficients for the renormalization. See text.

that the best-fit model parameters and the final results are not sensitive to moderate changes of the renormalization factors (Ranc et al. 2019). The data sets and the renormalization coefficients used in our analysis are summarized in Table 1.

Figure 1 shows the light curve from the OGLE and MOA data for OGLE-2014-BLG-0319. Prior to the peak of the event, a significant deviation of the light curve from a standard single-lens single-source (1L1S; Paczynski 1986) model was observed around HJD′ = 6772.[21] The anomaly was not noticed in real time and was first announced on 2014 April 30 (HJD′ = 6778) when the deviation almost finished so that any follow-up observations were not conducted during the anomaly. However, the deviation lasted about 10 days and both the OGLE and MOA regular observations could measure the deviation. After that, some modelers in survey groups immediately performed binary-lens modeling for this event using the light curves produced by their real-time photometry pipelines that return relatively rough DIA photometry.[22,23] D. P. Bennett, one of the modelers, suggested in their private communication on 2014 May 17 that the anomaly could be explained with planetary-mass-ratio models, although there is a potential model degeneracy, i.e., several competing models exist.

3. Light-curve Modeling

As shown in Figure 1, the light curve of OGLE-2014-BLG-0319 shows a significant deviation from a Paczynski (1986) single-lens single-source (1L1S) model. Such a deviation could be produced by a single-lens binary-source (1L2S) model (Gaudi 1998; Shin et al. 2019). However, we find that this 1L2S scenario is not preferred by $\Delta\chi^2 > 170$ comparing with the best-fit binary-lens single-source (2L1S) model.[24] The anomaly comprises the bump and dip parts deviating from the 1L1S model, and is well separated from the peak of the light curve, which implies the anomaly is likely due to the source crossing over or near planetary caustics.

Here, we present an exploration of the best-fit model to explain the nature of OGLE-2014-BLG-0319. Our light-curve modeling is done by our implementations of the image centered ray-shooting method (Bennett & Rhie 1996; Bennett 2010) and the Markov Chain Monte Carlo (MCMC) technique (Verde et al. 2003). In our analysis, we use a linear limb-darkening model for the source star. We apply the linear limb-darkening coefficients as $u_I = 0.5880$ and $u_{\rm MOA-Red} = 0.63445$, which are based on the extinction-corrected source color described in Section 4.1 and the ATLAS model (Claret & Bloemen 2011).

[21] HJD′ = HJD − 2, 450, 000.
[22] MOA, http://www.massey.ac.nz/~iabond/moa/alerts/.
[23] OGLE, http://ogle.astrouw.edu.pl/ogle4/ews/ews.html.
[24] The χ^2 differences between the 2L1S and 1L1S models are ∼340 for all of the data and ∼220 only for the MOA data.

3.1. Heuristic Analysis

We first present a heuristic analysis to predict the binary-lens parameters that produce the anomaly (Gould & Loeb 1992; Hwang et al. 2018; Skowron et al. 2018). This analysis is useful for discussing the origin of the model degeneracy for this event. The 1L1S modeling yields the parameters $(t_0, t_{\rm eff}, t_{\rm E}) \sim (6788.0, 6.0, 35.9)$ days, where t_0 is the time when the source approaches closest to the lens, $t_{\rm E}$ is the Einstein radius crossing time, $t_{\rm eff} (\equiv u_0 t_{\rm E})$ is the effective event timescale, and u_0 is the impact parameter in units of the angular Einstein radius $\theta_{\rm E}$. From Figure 1, the perturbation is centered at $t_{\rm anom} \sim 6770.0$ and then $\tau_{\rm anom} \equiv (t_0 - t_{\rm anom})/t_{\rm E} \sim 0.45$. Therefore, if the perturbation is induced by a planet, the source position at the anomaly $u_{\rm anom}$ and the angle between the source trajectory and the binary axis α (Rattenbury et al. 2002) would be

$$u_{\rm anom} = \sqrt{u_0^2 + \tau_{\rm anom}^2} \sim 0.53$$
$$\alpha = \tan^{-1}\left(\frac{u_0}{\tau_{\rm anom}}\right) \sim 18.^{\circ}3.$$

The projected separation between the lens host and planet in units of $\theta_{\rm E}$, s, can be estimated by $s - s^{-1} = u_{\rm anom}$, and then we approximately estimate $s \sim 0.77$ and 1.30. This estimation is based on the assumption that the perturbation was induced by the source directly crossing over the planetary caustics.

The remaining binary-lens parameters are (q, ρ), where q is the planet/host mass ratio and ρ is the source angular radius in units of $\theta_{\rm E}$. There are no sharp caustic-crossing features in the light curve, so we expect two cases: (1) the source directly passes over the planetary caustic and then fully or partially envelops the caustic (i.e., $q/\rho^2 \leqslant 1$), and (2) the source passes near the caustic. Here, we consider case 1 and then estimate $\rho \simeq t_{\rm bump}/2t_{\rm E} = 0.04$, where $t_{\rm bump} = 3$ days is the duration of the first bump in the anomaly. Under assumptions that the source is much larger than the Einstein radius of the planet $\theta_{\rm E,p} (\equiv \sqrt{q}\,\theta_{\rm E})$ and $s > 1$, the maximum excess magnification is $\Delta A = 2q/\rho^2$ (Gould & Gaucherel 1997). In this case, we estimate $q \sim 3 \times 10^{-4}$, where $\Delta A = 0.3$. This result implies that the anomaly was caused by a sub-Jovian-mass-ratio planet.

The heuristic analysis presented above is incomplete because it is based on several assumptions and we do not consider the case in which the source does not directly cross over the caustic. In order to avoid missing any 2L1S solutions for the event, we conduct a detailed grid search analysis in the next section. However, as discussed in Section 3.3, this heuristic analysis will help us understand the origin of the model degeneracy that we will find.

3.2. Grid Search Analysis

In order to avoid missing any local 2L1S solutions for the event, we conducted a grid search over the (q, s, α) parameter space where these three parameters are known to strongly affect the magnification pattern. We set $40 \times 40 \times 60 = 96{,}000$ grid points distributed at equal intervals over the search ranges of $-6 \leqslant \log q \leqslant 0, -1 \leqslant \log s \leqslant 1$, and $0 \leqslant \alpha < 2\pi$, respectively, and then we ran MCMC samplers at each grid point allowing all of the parameters to vary except for (q, s, α). The initial parameters of $(t_0, t_{\rm E}, u_0)$ are randomly set to be within the uncertainties of the 1L1S model. The source radius crossing time, $t_* (= \rho t_{\rm E})$, is also an important parameter for the magnification pattern (e.g., Bennett et al. 2008, 2014), so we randomly set an

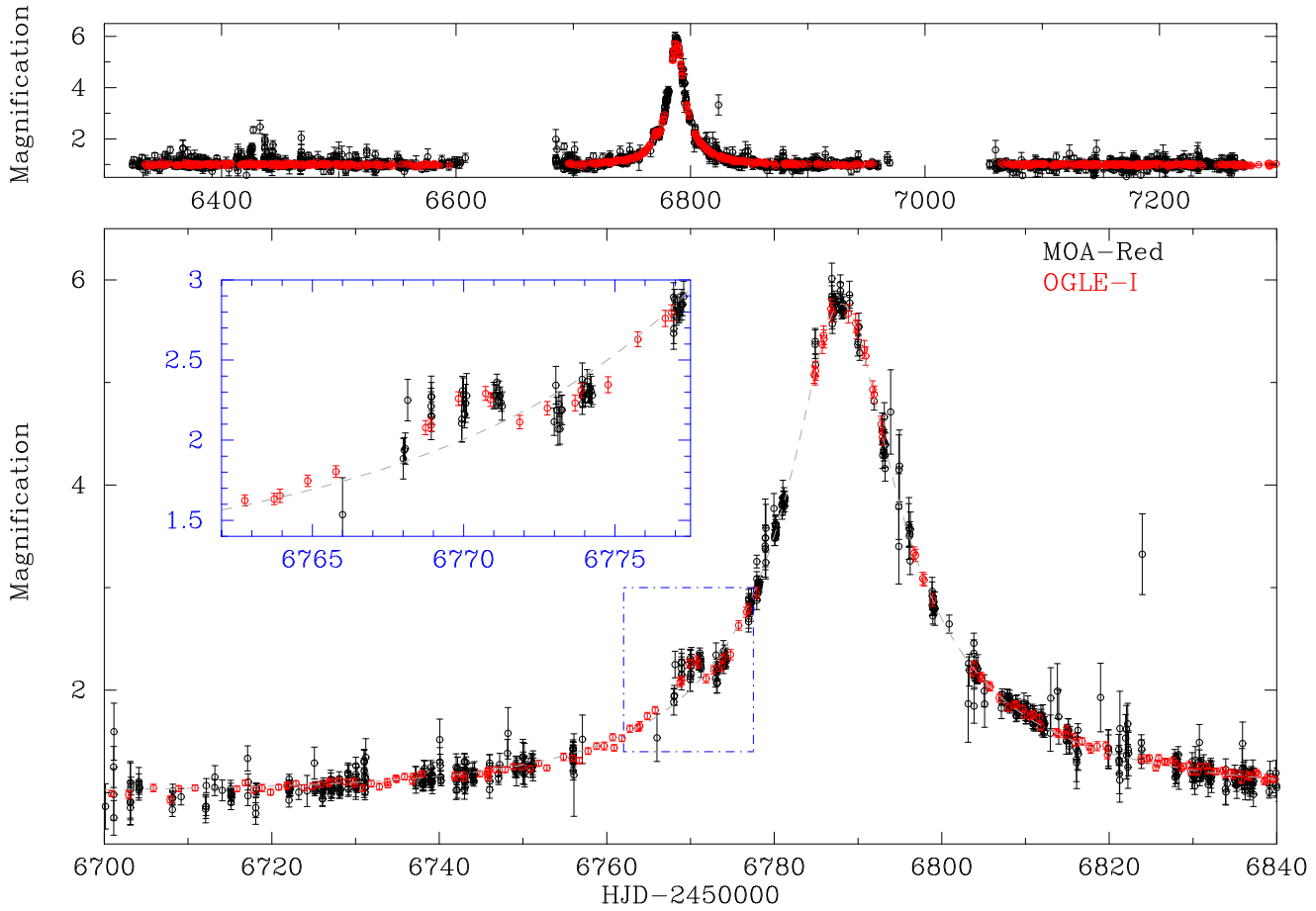

Figure 1. Light curve of OGLE-2014-BLG-0319 from the OGLE (red points) and MOA (black points) data. The gray dashed lines in panels represent the best-fit single-lens model. The blue panel shows a zoom-in view corresponding to the area surrounded by a blue chain line.

initial value of ρ at each grid point over $10^{-5} < \rho < 0.08$. After that, we refined all of the possible models by allowing all of the parameters to vary and then excluded models with $\Delta\chi^2 > 100$ compared to the best-fit model.

Our detailed grid search analysis found three different local minima for the 2L1S model. Here, we label the three models in the ranked order of the χ^2 goodness-of-fit values as "model A," "model B," and "model C." The model parameters and χ^2 values for each model are summarized in Table 2. Figure 2 allows a comparison between the three degenerate models. As shown in Figure 2, all of the three models fit the light-curve perturbation by having the sources cross near or over the planetary caustics, and model A is preferred over models B and C by $\Delta\chi^2 = 7.5$ and 18.4, respectively. We also tried to fit these models including high-order microlensing effects, parallax (Gould 2004; Muraki et al. 2011), xallarap (Poindexter et al. 2005; Miyazaki et al. 2021), and lens-orbital motion (Skowron et al. 2011). However, we found that these effects are not significant for this event and we could not obtain any meaningful constraints from the effects. This is probably because the effects are expected to be weak due to the relatively short timescale $t_E \sim 30$ days and large impact parameter $u_0 \sim 0.2$.[25]

[25] Moreover, we found the baseline variability of the light curve remains even if we tried to remove it, which can systematically affect our secure measurements of the high-order effects. Therefore, we focus on the static models.

Table 2
Binary-lens Model Parameters

Parameters (Units)	Model A	Model B	Model C
t_0 (HJD′ − 6780)	$7.963^{+0.025}_{-0.025}$	$8.035^{+0.024}_{-0.023}$	$8.045^{+0.024}_{-0.024}$
t_E (days)	$34.46^{+0.46}_{-0.47}$	$34.74^{+0.41}_{-0.43}$	$34.79^{+0.48}_{-0.45}$
u_0	$0.174^{+0.003}_{-0.003}$	$0.175^{+0.003}_{-0.003}$	$0.171^{+0.003}_{-0.003}$
q ($\times 10^{-4}$)	$10.34^{+1.31}_{-1.11}$	$6.56^{+0.61}_{-0.53}$	$4.51^{+0.87}_{-0.77}$
s	$1.213^{+0.005}_{-0.006}$	$0.762^{+0.003}_{-0.003}$	$1.287^{+0.005}_{-0.005}$
α (radians)	$2.834^{+0.003}_{-0.003}$	$5.845^{+0.006}_{-0.006}$	$2.859^{+0.005}_{-0.005}$
ρ ($\times 10^{-2}$)	<2.7[a]	$3.95^{+0.31}_{-0.26}$	$2.82^{+0.39}_{-0.34}$
t_* (days)	<0.78[a]	$1.37^{+0.10}_{-0.09}$	$0.98^{+0.13}_{-0.12}$
Best-fit χ^2	3867.93	3875.41	3886.31
$\Delta\chi^2$	…	7.48	18.38

Note. Medians of the MCMC posterior distributions with uncertainties corresponding to the 68% credible intervals around the medians.
[a] The 3σ upper limit.

3.3. Origin of the Degeneracy

Here, we discuss the origin of the model degeneracy found in the previous section. In Section 3.1, we estimated $s \sim 0.77$ and 1.30 based on the assumption that the source directly crosses over the planetary caustic. Models B and C would enter into the group of models we predicted given that in them the source crosses over the caustic and the value of s is similar. As expected, given there were no sharp caustic-crossing features in the anomaly, the source

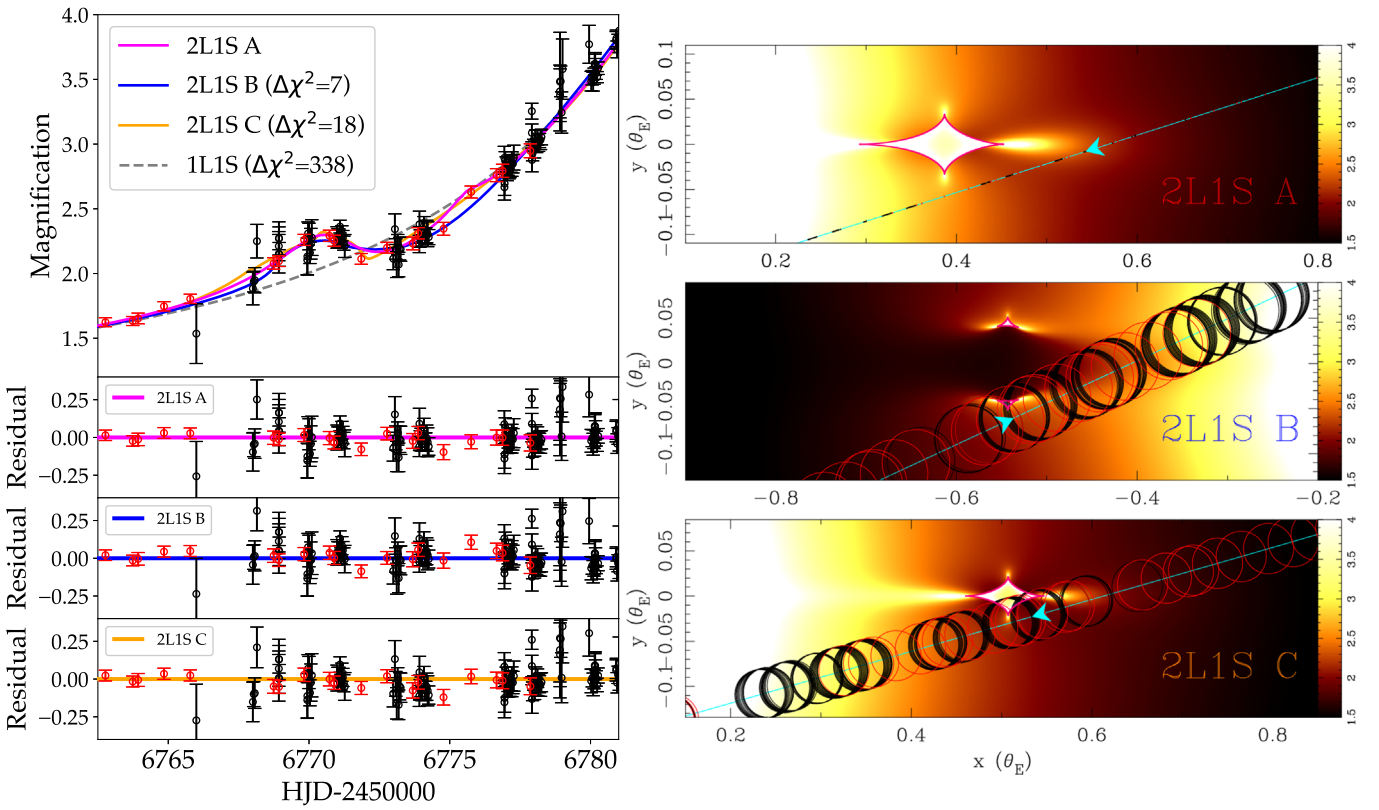

Figure 2. Comparison of the three local solutions, models A, B, and C. Left: a detailed view of the light curves when the anomaly occurred. Each 2L1S model curve is presented by a colored solid line and the 1L1S model curve is shown as a dashed gray line. The black and red circles with error bars are the light curves of MOA and OGLE, respectively. Right: the three panels show the geometries of planetary caustics (magenta solid lines) relative to the source trajectories (cyan solid lines) for each model. The cyan arrows indicate the directions in which the source is moving. The black and red circles represent the source positions when the MOA and OGLE measurements were conducted. The sizes of the circles are the best-fit source size of each model. The magnification maps are represented as color maps in each panel.

sizes for both models are relatively large compared to the caustics, as is shown in the right panels of Figure 2, and the source sizes are well constrained. That said, we found model A, with a significantly smaller source size, provides a somewhat better fit. This model can be considered as the case we did not consider in Section 3.1. In this case, the source crosses near the planetary caustic to reproduce the smooth perturbation. To illuminate this discussion, we introduce the parameter (Hwang et al. 2018)

$$|\Delta\xi| = |u_0 \csc\alpha' - \xi_{\pm}|, \tag{1}$$

where $\alpha' = \alpha \pm n\pi$ is defined to satisfy $\alpha' < \frac{\pi}{2}$ and $\xi_{\pm} = |s - s^{-1}|$. Hence, $|\Delta\xi|$ approximately represents the distance between the center of the source and the caustic when the source crosses the binary-lens axis. Figure 3 represents the MCMC distribution colored by $\Delta\chi^2$ for each model on the ($|\Delta\xi|$, t_*), ($|\Delta\xi|$, $\log q$), and ($\log s$, $\log q$) planes. One sees that the three models seem continuous in the ($|\Delta\xi|$, $\log q$) plane. However, model A is clearly separated from models B and C on the ($|\Delta\xi|$, t_*) plane, and we note that models B and C are well separated on ($\log s$, $\log q$) plane. Therefore, the three models are discrete in the microlensing parameter spaces and are thus distinguishable. Although the model degeneracy for the event is within our expectations from the heuristic analysis and the visual inspection of the light curve, the degeneracy is worth discussing.

A first degeneracy is between models with $s > 1$ and $s < 1$ at planetary-caustic perturbations, i.e., the degeneracy between models B and C for this event. In general, the degeneracy could be resolvable because the caustic structures between them are qualitatively quite different and the light-curve features and the timing of the anomalies are different enough to distinguish them. The reason why the degeneracy occurred in this event would be due to the large source radii that "wash out" the magnification patterns such that both models reproduce similar magnification patterns. Gaudi & Gould (1997) also predict such a degeneracy; see their Figure 1. Recently, Zang et al. (2021a) also encountered a similar degeneracy in a planetary event with $q \sim 10^{-5}$ and $\rho \sim 10^{-3}$. A second degeneracy is between models with sources crossing near the caustic and models with large sources crossing over the caustic, i.e., the degeneracy between models A and C for this event. This degeneracy was also found in Zang et al. (2020). In this degeneracy, one can constrain the source size, which is relatively large compared with the caustic, and the other cannot, which is also demonstrated in Zang et al. (2020). This is qualitatively possible for planetary-caustic events with no sharp caustic-crossing features.

4. Physical Properties

The angular Einstein radius $\theta_{\rm E}$ provides the important mass −distance relation for the lens system:

$$M_L = \frac{c^2}{4G}\theta_{\rm E}^2 \frac{D_S D_L}{D_S - D_L}, \tag{2}$$

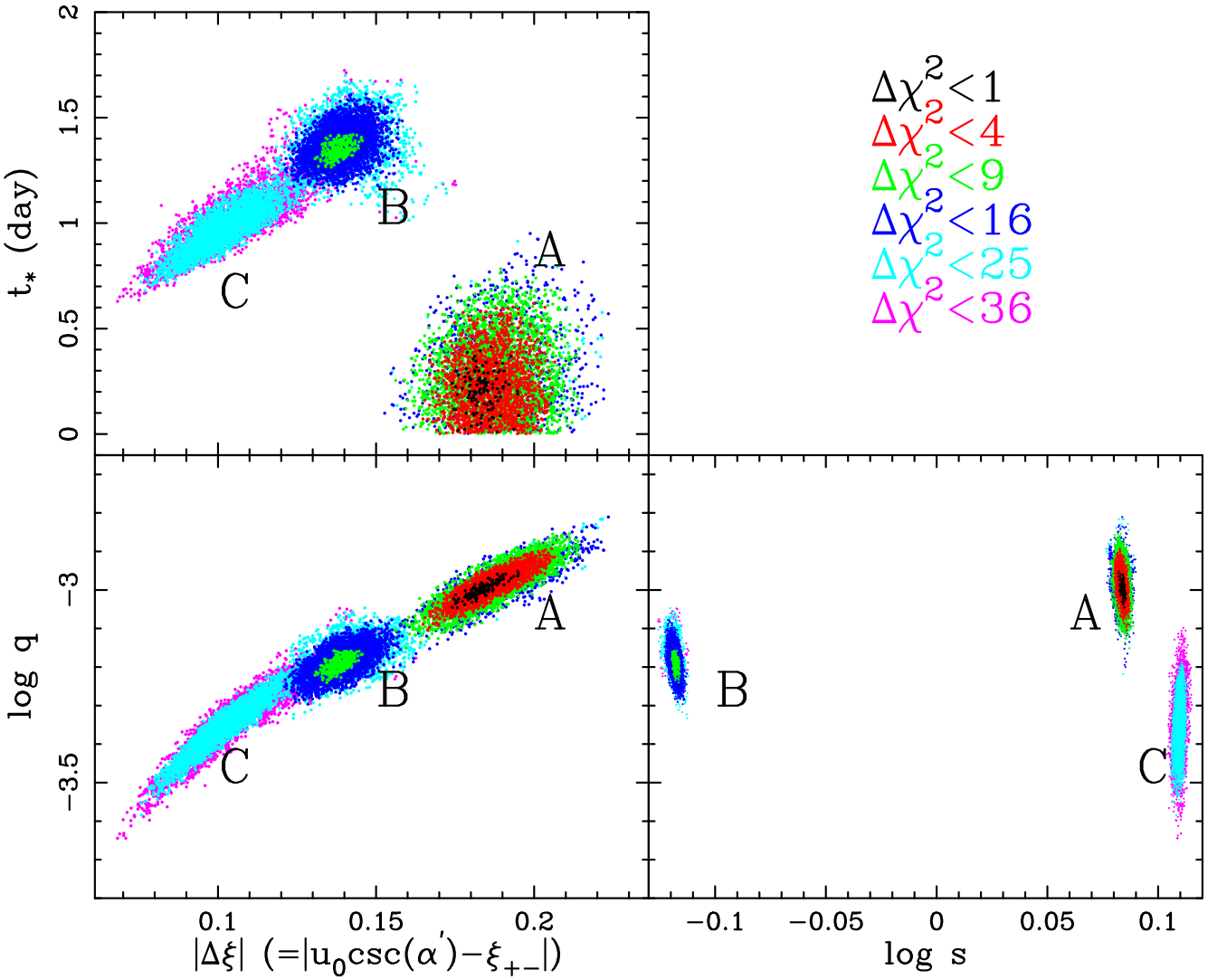

Figure 3. The $\Delta\chi^2$ distribution in the MCMC chains on ($|\Delta\xi|$, t_*), ($|\Delta\xi|$, $\log q$), and ($\log s$, $\log q$) planes for each model, where the points of black, red, green, blue, cyan, and magenta represent the MCMC links with $\Delta\chi^2 < (1, 4, 9, 16, 25, 36)$, respectively.

where D_S and D_L are the distances of the source and the lens from the observer, respectively. In order to determine $\theta_{\rm E}$, we measure the angular source radius $\theta_* (\equiv \rho\theta_{\rm E})$, which can be estimated from its color and magnitude (Boyajian et al. 2014).

4.1. Source Property

As mentioned in Section 2, we do not have any measurements in the V band for this event. The source magnitudes in the I band (I_S) and the MOA-Red band ($R_{M,S}$) are precisely measured from the light-curve analysis and these enable us to estimate the source color of $(V-I)$ using an empirical color–color relation between $(R_M - I)$ and $(V-I)$; (Gould et al. 2010; Bennett et al. 2012). We note that the MOA light curve is scaled to match the instrumental MOA-II DOPHOT catalog (Bond et al. 2017) and the OGLE light curve is calibrated to the standard Cousins I band.

We extracted isolated and relatively bright stars in the OGLE-III catalog that are located within a $2'$ circle centered on the event and then cross-referenced the stars in the MOA-II catalog. We removed stars with colors $(V-I) < 2.0$ and then derived the following relation using an MCMC algorithm with 144 cross-matched stars:

$$R_M - I = (0.196^{+0.026}_{-0.027})(V-I) - 28.112^{+0.067}_{-0.068},$$

where the parameter uncertainties for the slope and intercept correspond to the 1σ credible intervals around the median values in the MCMC stationary distribution. In the bottom panel of Figure 4, we show 300 relations (blue translucent lines) randomly extracted from the MCMC distribution. There is a strong correlation between the slope and intercept parameters in the MCMC distribution. Using the color–color relation, we estimated the source color and magnitude to be $(V-I, I)_S = (2.643, 17.829) \pm (0.046, 0.004)$ for model A. We note that the uncertainty of the source color $(V-I)_S$ largely comes from the uncertainty of the color–color relation.

Figure 4 also shows the $(V-I, I)$ color–magnitude diagram (CMD) of the OGLE-III catalog within $2'$ of the event, which is calibrated to the standard photometric system (Szymański et al. 2011). We also plot the CMD of the Hubble Space Telescope (HST) catalog (Holtzman et al. 1998) and found that the source color is somewhat redder than a subgiant group in the Galactic Bulge. We estimated the average color of the subgiant group in

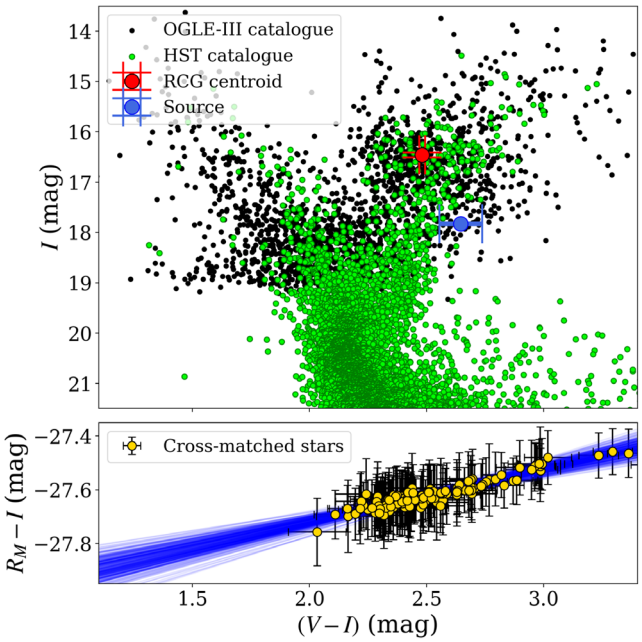

Figure 4. Top: the $(V-I, I)$ color–magnitude diagram (CMD) in the standard Kron−Cousins I and Johnson V photometric system. The positions of the Red Clump (RC) centroid and the source are presented as the red and blue circles. The black dots indicate stars of the OGLE-III catalog within 2′ of the event. The green circles indicate the Hubble Space Telescope (HST) catalog (Holtzman et al. 1998), whose position is matched using the RC centroid. Bottom: the empirical color–color relation between the standard system $(V-I)$ and instrumental color $(R_{\rm MOA}-I)$. The blue translucent lines are 300 samples randomly extracted from the MCMC distribution.

the HST CMD following Bennett et al. (2008) as $(V-I)_{\rm HST} = 2.43 \pm 0.11$ and confirmed that this is consistent with $(V-I)_S$ at 2σ. To be consistent with each color, we doubled the nominal error bars on the source color and thus adopted $(V-I)_S = 2.643 \pm 0.093$ in later analysis. Then, we estimated the position of the RC centroid in the CMD to be $(V-I,\ I)_{\rm RC} = (2.481,\ 16.464) \pm (0.013,\ 0.050)$. Comparing $(V-I,\ I)_{\rm RC}$ with the intrinsic RC color and magnitude $(V-I,\ I)_{\rm RC,0} = (1.060,\ 14.605) \pm (0.060,\ 0.040)$; (Bensby et al. 2013; Nataf et al. 2013), we estimated the RC reddening and extinction to be $E(V-I)_{\rm RC} = 1.421 \pm 0.061$ and $A_{I,\rm RC} = 1.856 \pm 0.064$, respectively, and then derived the extinction-corrected source color and magnitude $(V-I,\ I)_{S,0} = (1.223,\ 15.973) \pm (0.111,\ 0.064)$ on the assumption that the source suffers the same extinction as the RC in the Bulge (Yoo et al. 2004).

Using the intrinsic source color and magnitude and the following empirical relation (Boyajian et al. 2014):

$$\log(2\theta_*/{\rm mas}) = 0.5014 + 0.4197(V-I)_{S,0} - 0.2I_{S,0},$$

we derived the angular source radius $\theta_* = 3.303 \pm 0.374\ \mu$as for model A. We summarize the source properties for each model in Table 3.

4.2. Angular Einstein Radius

Finally, we estimated the angular Einstein radius $\theta_{\rm E}(\equiv \theta_*/\rho)$ and the lens-source relative proper motion $\mu_{\rm rel}(\equiv \theta_{\rm E}/t_{\rm E})$ to be

$$\theta_{\rm E}/({\rm mas}) = \begin{cases} >0.124 & \text{(for Model A)} \\ 0.086 \pm 0.012 & \text{(for Model B)}, \\ 0.116 \pm 0.020 & \text{(for Model C)} \end{cases}$$

Table 3
Source Properties

	Model A	Model B	Model C
$(V-I)_S$[a]	2.643 ± 0.093	2.675 ± 0.096	2.648 ± 0.093
I_S	17.829 ± 0.004	17.846 ± 0.004	17.868 ± 0.004
$(V-I)_{S,0}$	1.223 ± 0.111	1.254 ± 0.114	1.228 ± 0.111
$I_{S,0}$	15.973 ± 0.064	15.990 ± 0.064	16.012 ± 0.064
θ_* (μas)	3.303 ± 0.374	3.378 ± 0.390	3.261 ± 0.370

Note. $(V-I)_S$: apparent color; I_S: apparent magnitude; $(V-I)_{S,0}$: extinction-free color; $I_{S,0}$: extinction-free magnitude; θ_*: angular radius.
[a] The error bars are extended to be consistent with the average color of a subgiant group in the HST CMD.

and

$$\mu_{\rm rel}/({\rm mas\ yr^{-1}}) = \begin{cases} >1.316 & \text{(for Model A)} \\ 0.90 \pm 0.12 & \text{(for Model B)}, \\ 1.21 \pm 0.21 & \text{(for Model C)} \end{cases}$$

respectively. We note that the limit for model A is the 3σ.

These observed angular Einstein radii for each model provide important constraints on the lens mass M_L and relative lens-source parallax $\pi_{\rm rel} \equiv {\rm au}(D_L^{-1} - D_S^{-1})$, as

$$M_L = \frac{\theta_{\rm E}^2}{\kappa \pi_{\rm rel}} = \begin{Bmatrix} >0.063 \\ 0.030 \\ 0.055 \end{Bmatrix} M_\odot \left(\frac{0.03\ {\rm mas}}{\pi_{\rm rel}} \right), \quad (3)$$

where $\kappa = 8.144\ {\rm mas}\ M_\odot^{-1}$ and $\pi_{\rm rel} = 0.03$ mas is a typical value for lenses in the Galactic Bulge. This implies that the lenses for models B and C would be substellar objects, which is unlikely for microlensing events with $t_{\rm E} \sim 35$ days (Sumi et al. 2011; Mróz et al. 2017). To quantitatively demonstrate this, we compared the observed $\theta_{\rm E}$ and $\mu_{\rm rel}$ values with prior probabilities derived from a Bayesian analysis using a Galactic model optimized for use in microlensing studies (Koshimoto et al. 2021a), detailed in the Section 4.3. Figure 5 shows the result and indicates that the observed $\theta_{\rm E}$ and $\mu_{\rm rel}$ values for models B and C are $\sim 3\sigma$ from the medians. Therefore, we conclude that models B and C are unlikely candidates for the best solution. This is in addition to the fact that they have worse χ^2 values.[26] We therefore conclude that model A is the best solution for the event. However, we should note that the prior probabilities presented in Figure 5 do not consider the planet-hosting probability that is likely dependent on properties of the host star, such as mass, metallicity, and its Galactic location. A recent statistical study using 28 planetary events indicates that the dependence on Galactic location might be small, however (Koshimoto et al. 2021b). For completeness, we summarize the final results of models B and C in the Appendix.

4.3. Bayesian Analysis

Because we cannot obtain any significant parallax measurements, we cannot directly determine the physical properties of the lens system. Therefore, we conducted a Bayesian analysis in order to quantitatively estimate the probability distribution of the physical properties. We employed a new parametric

[26] Under the assumption of a normal distribution, models B and C can be rejected at significance levels of ~ 0.02 and $\sim 10^{-4}$, respectively.

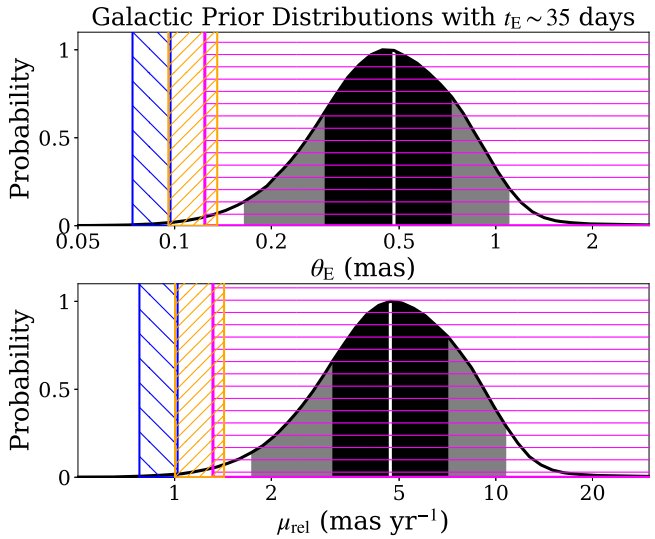

Figure 5. Prior probabilities of θ_E and μ_{rel} derived from a standard Galactic model, where the black and gray regions indicate the 68.3% (1σ) and 95.4% (2σ) credible intervals and the vertical white lines indicate the median values. Here, the prior probabilities are weighted by the observed probability distribution of $t_E \sim 35$ days. The hatched region colored in magenta represents the 3σ region for model A. Also, the regions colored in blue and orange represent the 1σ regions for models B and C, respectively. The measured θ_E and μ_{rel} for models B and C are unreasonably small compared with the prior probabilities.

Galactic model developed to match recent various observation data toward the Galactic Bulge. We generated $\sim 10^6$ artificial microlensing events using the public code `genulens`[27] (Koshimoto & Ranc 2021). We then derived the posterior probability distribution weighting by the observed likelihood distributions of t_E, θ_E, I_S, and $(V-I)_S$. The result of the Bayesian analysis is shown in Figure 6 and the physical parameters derived are summarized in Table 4. The analysis indicates that the lens system comprises a sub-Jovian-mass planet orbiting an M-dwarf star near the Galactic Bulge.

4.4. Future Follow-up Observations

Future follow-up observations with high angular resolution might be able to give an additional mass−distance relation derived from the lens flux. This can resolve the large uncertainties of the lens physical parameters (Bennett et al. 2015; Bhattacharya et al. 2018; Bennett et al. 2020; Bhattacharya et al. 2020; Vandorou et al. 2020; Terry et al. 2021). For this, we also estimated the apparent magnitude of the lens brightness in the Bayesian analysis. Here, we modeled the extinction in front of the lens (Bennett et al. 2015) as

$$A_L = \frac{1 - e^{-D_L/(0.1\mathrm{kpc})\sin|b|}}{1 - e^{-D_S/(0.1\mathrm{kpc})\sin|b|}} A_S \quad (4)$$

where A_L and A_S are the extinction values for the lens and source systems, respectively. We used the mass–luminosity and color–color relations (Henry & McCarthy 1993; Kroupa et al. 1993; Kenyon & Hartmann 1995) and the extinction law (Nishiyama et al. 2009) to derive the apparent magnitudes of the lens and the source in different passbands. The result is summarized in Table 4. It is expected that the source is ∼5.1 mag brighter than the lens in the K band and the angular separation between the source and the lens will be ∼35 mas in 2022. Owing to such a high contrast, several more years might need to pass in order to resolve the lens position and detect the lens flux. However, observing the lens not only can resolve the uncertainties of the physical parameters, it can also break the model degeneracy because each degenerate model indicates different lens-source relative proper motions μ_{rel}. Therefore, it would be worth conducting these future follow-up observations.

[27] https://github.com/nkoshimoto/genulens

5. Summary and Discussion

We present the analysis of the planetary microlensing event OGLE-2014-BLG-0319. We find three possible models with different mass ratios $q = (10.3,\ 6.6,\ 4.5) \times 10^{-4}$ and lens-source relative proper motions $\mu_{rel} = (>2.50,\ 0.90,\ 1.26)$ mas yr^{-1}, respectively. We rule out the last two models with small μ_{rel} values considering the Galactic prior probability. Finally, we conduct a Bayesian analysis using a Galactic model and estimate that the lens system consists of a sub-Jupiter-mass planet orbiting an M dwarf near the Galactic Bulge.

5.1. Degeneracy of Mass Ratios and Proper Motions

In general, the mass ratio q is approximately determined from the duration of planetary perturbation relative to t_E. If the source size is large relative to the Einstein radius of the planet, then the duration of the perturbation becomes the source crossing time. Gaudi & Gould (1997) predict a continuous degeneracy in such a case: $\mu_{rel}\rho q^{1/2} = const$. At a given μ_{rel}, the $q^{1/2}$ and ρ can be degenerate. They also propose that the low-mass solutions with low μ_{rel} values could be a priori ruled out. For the event OGLE-2014-BLG-0319, we can rule out models B and C by comparing the measured values and the Galactic prior probabilities for θ_E and μ_{rel}. This approach can be made because the observed values are unlikely at a given $t_E \sim 35$ days.[28] However, we expect this would be more difficult for short-timescale (low-mass lens) events because $\rho \propto t_E^{-1}$ and $t_E \propto \sqrt{M_L}$. For example, a Bayesian analysis with $t_E \sim 5$ days provides high prior probabilities at $\theta_E \sim 0.1$ mas and $\mu_{rel} \sim 1$ mas yr^{-1}.

So far, there have been several reported short-timescale events that suffered from similar model degeneracies between different q and μ_{rel} values (e.g., Miyazaki et al. 2018; Zhang et al. 2020). These events have several degenerate solutions with $\rho \geqslant 0.01$ and $t_E \leqslant 10$ days and they cannot be ruled out by Galactic priors. As discussed in Zhang et al. (2020), the discovery rate of short-timescale events with planetary (short-lived) perturbations has greatly increased since current second-generation microlensing surveys started. Hence, we can now explore planets around low-mass dwarfs, brown dwarfs, and even planetary-mass objects. However, the degeneracy would be more common for short-timescale events and thus might have large impacts on the estimation for the frequency of such planets.

5.2. Detection Efficiency Dependence on Source Size

Furthermore, estimating different ρ values can lead to different detection efficiencies of planets for each event.

[28] Interestingly, Han et al. (2020) reported a discovery of a planetary microlensing event with $t_E = 45$ days and $\mu_{rel} \sim 0.79$ mas yr^{-1}. Note that they confirmed that there are no competing models with the final result.

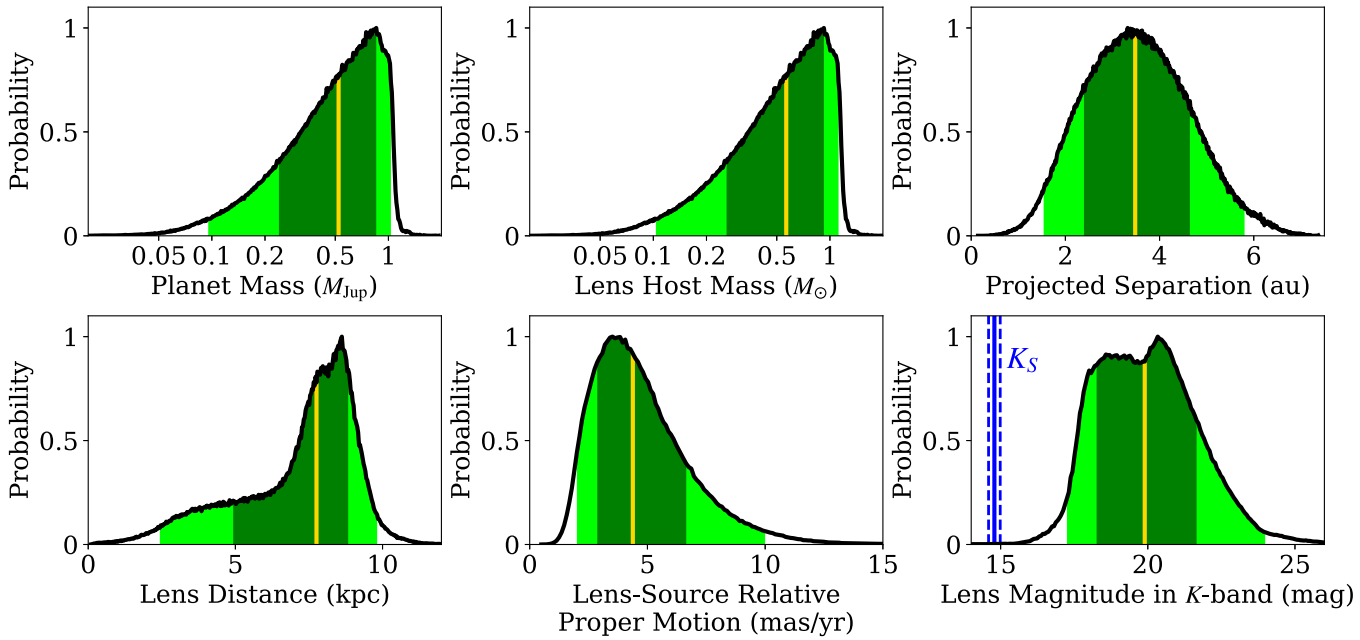

Figure 6. Posterior probability distributions of the physical parameters derived from a Bayesian analysis using a Galactic model. The green and light green regions indicate the 68.3% (1σ) and 95.4% (2σ) credible intervals and the vertical yellow lines indicate the median values. We also plot the expected source magnitude K_S in the lower right panel where the dashed lines indicate the 1σ uncertainties.

Table 4
Physical Parameters

Physical Parameters (Units)	Median $\pm$ 1σ
Planet Mass, M_P ($M_{\rm Jup}$)	$0.57^{+0.36}_{-0.31}$
Lens Host Mass, $M_{\rm Host}$ ($M_\odot$)	$0.52^{+0.33}_{-0.29}$
Projected Semimajor Axis, $a_\perp$ (au)	$3.49^{+1.17}_{-1.12}$
Distance to the Lens System, D_L (kpc)	$7.73^{+1.14}_{-2.84}$
Distance to the Source, D_S (kpc)	$10.30^{+3.35}_{-0.68}$
Angular Einstein Radius, $\theta_{\rm E}$ (mas)	$0.41^{+0.22}_{-0.15}$
Lens-Source Proper Motion, $\mu_{\rm rel}$ (mas yr^{-1})	$4.38^{+2.32}_{-1.62}$
Lens Magnitude in I Band, I_L (mag)	$23.43^{+2.23}_{-2.26}$
Lens Magnitude in H Band, H_L (mag)	$20.29^{+1.86}_{-1.81}$
Lens Magnitude in K Band, K_L (mag)	$19.92^{+1.79}_{-1.70}$
Source Magnitude in H Band, H_S (mag)	15.04 ± 0.20
Source Magnitude in K Band, K_S (mag)	14.79 ± 0.20

Figure 7 shows the planet detection efficiencies for each model as a function of $\log q$, in which the dashed vertical lines represent the observed q for each model (details of the calculation for the detection efficiency are similar to that in Suzuki et al. 2016; see their Section 4). For this event, the different ρ estimation for each model does not strongly affect the efficiency at $\log q \sim -3$. However, the effect would be more serious at $\log q \ll -3$ where the detection efficiencies are different by an order of magnitude, as shown in Figure 7. This indicates that the detection efficiency of low mass-ratio planets around low-mass objects would largely be dependent on $\rho\,(\equiv \theta_*/\mu_{\rm rel} t_{\rm E})$ and calls our attention to some assumptions used to estimate the detection efficiency. Recent planet discoveries with $q < 2 \times 10^{-5}$ have also shown that smaller ρ is more sensitive to low-mass planets: $\rho \sim 5 \times 10^{-4}$ (KMT-2018-BLG-0029, Gould et al. 2020), $\rho \sim 3 \times 10^{-4}$ (OGLE-2019-BLG-0960, Yee et al. 2021), $\rho \sim 2 \times 10^{-3}$ (OGLE-2019-BLG-1053, Zang et al. 2021b), and $\rho \sim 6 \times 10^{-4}$ (KMT-2020-BLG-0414, Zang et al. 2021a).

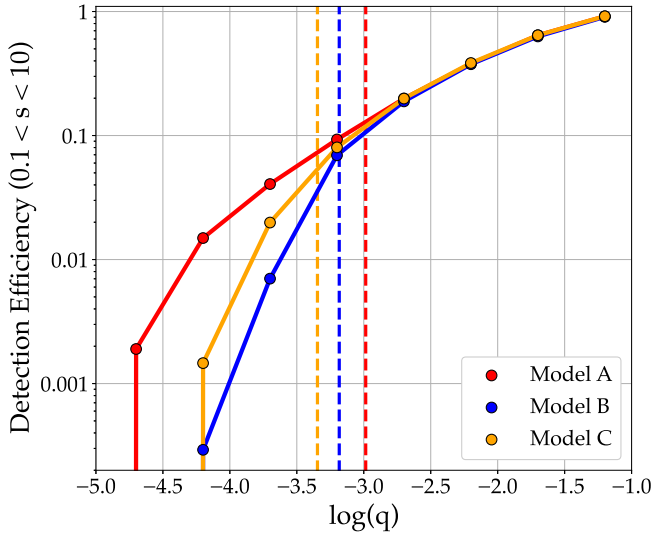

Figure 7. Detection efficiencies for each degenerate model as a function of mass ratio q. The vertical dashed lines represents the observed q for each model. For model A, we used the best-fit value of $\rho = 7.0 \times 10^{-3}$ for calculation.

For example, Suzuki et al. (2016) derived ρ values assuming that single-lens events have a $\mu_{\rm rel}$ distribution similar to that of their planetary sample, $\mu_{\rm rel} = 5.74^{+2.94}_{-2.84}$ mas yr^{-1}, and then calculated the detection efficiency for each event.[29] They demonstrated that the efficiency does not significantly depend on the derived ρ values within the 1σ uncertainties (see Figure 7 of Suzuki et al. 2016). Moreover, the $\mu_{\rm rel}$ distribution they assumed is also consistent with the prediction of a Galactic model. However, it is unclear whether the assumption holds up

[29] Note that they calculated the detection efficiencies for each single-lens event using a value of $\mu_{\rm rel} = 5.6$ mas yr^{-1} so that their final result does not include the uncertainties of $\mu_{\rm rel}$. However, they showed it hardly affects the final result.

Table 5
Physical Parameters for Models B and C

Physical Parameters (Units)	Model B	Model C
Planet Mass, M_P ($M_\oplus$)	$17.05^{+25.71}_{-9.45}$	$17.14^{+24.35}_{-8.48}$
Lens Host Mass, $M_{\rm Host}$ ($M_\odot$)	$0.08^{+0.12}_{-0.04}$	$0.11^{+0.16}_{-0.06}$
Projected Semimajor Axis, $a_\perp$ (au)	$0.64^{+0.10}_{-0.09}$	$1.45^{+0.27}_{-0.24}$
Distance to the Lens System, D_L (kpc)	$8.96^{+0.55}_{-0.63}$	$8.92^{+0.57}_{-0.71}$
Distance to the Source, D_S (kpc)	$10.12^{+1.85}_{-0.63}$	$10.29^{+1.67}_{-0.65}$
Angular Einstein Radius, $\theta_{\rm E}$ (mas)	$0.10^{+0.01}_{-0.02}$	$0.13^{+0.02}_{-0.02}$
Lens-Source Proper Motion, $\mu_{\rm rel}$ (mas yr^{-1})	$0.97^{+0.12}_{-0.12}$	$1.32^{+0.20}_{-0.19}$
Lens Magnitude in I Band, I_L (mag)	$28.29^{+2.68}_{-2.12}$	$27.83^{+2.30}_{-2.04}$
Lens Magnitude in H Band, H_L (mag)	$26.61^{+6.16}_{-3.27}$	$24.51^{+5.89}_{-1.92}$
Lens Magnitude in K Band, K_L (mag)	$26.07^{+7.66}_{-3.21}$	$24.02^{+6.31}_{-1.89}$
Source Magnitude in H Band, H_S (mag)	15.04 ± 0.20	15.08 ± 0.20
Source Magnitude in K Band, K_S (mag)	14.78 ± 0.20	14.82 ± 0.20

in the low-mass regime because the Galactic model for low-mass objects such as for their velocity distribution is still much less clear and might differ from that for objects in the stellar-mass regime (Sajadian et al. 2021). Considering this effect could be important in the estimation of the frequency of planets around low-mass dwarfs, brown dwarfs (Lingam et al. 2020), and even moons around free-floating planets (Bennett et al. 2014). This would be effectively investigated by the Roman Galactic Exoplanet Survey (RGES; Penny et al. 2019; Johnson et al. 2020), which has much better sensitivity to short-timescale events than current microlensing surveys.

We appreciate the anonymous referee for helping to improve the paper. We acknowledge the following support. Work by S.M. is supported by JSPS KAKENHI grant No. 21J11296. The work of D.P.B., N.K., C.R., Y.H., and A.B. was supported by NASA under award No. 80GSFC17M0002. C.R. is supported by the ANR project COLD-WORLDS of the French Agence Nationale de la Recherche with the reference ANR-18-CE31-0002. The MOA project is supported by JSPS KAKENHI grant Nos. 19KK0082 and 20H04754.

Appendix
Physical Parameters for Models B and C

For completeness, we present Table 5, which represents the physical parameters for models B and C derived by the Bayesian analysis presented in Section 4.3.

ORCID iDs

Shota Miyazaki https://orcid.org/0000-0001-9818-1513
Daisuke Suzuki https://orcid.org/0000-0001-9818-1513
Andrzej Udalski https://orcid.org/0000-0001-5207-5619
Naoki Koshimoto https://orcid.org/0000-0003-2302-9562
David P. Bennett https://orcid.org/0000-0001-8043-8413
Takahiro Sumi https://orcid.org/0000-0002-4035-5012
Nicholas Rattenbury https://orcid.org/0000-0001-5069-319X
Han Cheongho https://orcid.org/0000-0002-2641-9964
Richard K. Barry https://orcid.org/0000-0003-4916-0892
Akihiko Fukui https://orcid.org/0000-0002-4909-5763
Yuki Hirao https://orcid.org/0000-0003-4776-8618
Stela Ishitani Silva https://orcid.org/0000-0003-2267-1246
Yoshitaka Itow https://orcid.org/0000-0002-8198-1968
Iona Kondo https://orcid.org/0000-0002-3401-1029
Yasushi Muraki https://orcid.org/0000-0003-1978-2092
Greg Olmschenk https://orcid.org/0000-0001-8472-2219
Clément Ranc https://orcid.org/0000-0003-2388-4534
Jan Skowron https://orcid.org/0000-0002-2335-1730
Michal K. Szymański https://orcid.org/0000-0002-0548-8995
Igor Soszyński https://orcid.org/0000-0002-7777-0842
Pawel Pietrukowicz https://orcid.org/0000-0002-2339-5899
Krzysztof Ulaczyk https://orcid.org/0000-0001-6364-408X

References

Akeson, R. L., Chen, X., Ciardi, D., et al. 2013, PASP, 125, 989
Alard, C., & Lupton, R. H. 1998, ApJ, 503, 325
Bennett, D. P. 2010, ApJ, 716, 1408
Bennett, D. P., Batista, V., Bond, I. A., et al. 2014, ApJ, 785, 155
Bennett, D. P., Bhattacharya, A., Anderson, J., et al. 2015, ApJ, 808, 169
Bennett, D. P., Bhattacharya, A., Beaulieu, J.-P., et al. 2020, AJ, 159, 68
Bennett, D. P., Bond, I. A., Udalski, A., et al. 2008, ApJ, 684, 663
Bennett, D. P., Ranc, C., & Fernandes, R. B. 2021, AJ, 162, 243
Bennett, D. P., & Rhie, S. H. 1996, ApJ, 472, 660
Bennett, D. P., Sumi, T., Bond, I. A., et al. 2012, ApJ, 757, 119
Bensby, T., Yee, J. C., Feltzing, S., et al. 2013, A&A, 549, A147
Bhattacharya, A., Beaulieu, J. P., Bennett, D. P., et al. 2018, AJ, 156, 289
Bhattacharya, A., Bennett, D. P., Beaulieu, J. P., et al. 2020, arXiv:2009.02329
Bond, I. A., Abe, F., Dodd, R. J., et al. 2001, MNRAS, 327, 868
Bond, I. A., Bennett, D. P., Sumi, T., et al. 2017, MNRAS, 469, 2434
Boyajian, T. S., van Belle, G., & von Braun, K. 2014, AJ, 147, 47
Butler, R. P., Wright, J. T., Marcy, G. W., et al. 2006, ApJ, 646, 505
Charbonneau, D., Brown, T. M., Latham, D. W., & Mayor, M. 2000, ApJL, 529, L45
Claret, A., & Bloemen, S. 2011, A&A, 529, A75
Cumming, A., Butler, R. P., Marcy, G. W., et al. 2008, PASP, 120, 531
Fressin, F., Torres, G., Charbonneau, D., et al. 2013, ApJ, 766, 81
Gaudi, B. S. 1998, ApJ, 506, 533
Gaudi, B. S., & Gould, A. 1997, ApJ, 486, 85
Gould, A. 2004, ApJ, 606, 319
Gould, A., Dong, S., Bennett, D. P., et al. 2010, ApJ, 710, 1800
Gould, A., & Gaucherel, C. 1997, ApJ, 477, 580
Gould, A., & Loeb, A. 1992, ApJ, 396, 104
Gould, A., Ryu, Y.-H., Calchi Novati, S., et al. 2020, JKAS, 53, 9
Han, C., Bond, I. A., Gould, A., et al. 2018, AJ, 156, 226
Han, C., Udalsk, A., Gould, A., et al. 2020, AJ, 159, 91
Henry, T. J., & McCarthy, D. W. J. 1993, AJ, 106, 773
Holtzman, J. A., Watson, A. M., Baum, W. A., et al. 1998, AJ, 115, 1946
Howard, A. W., Marcy, G. W., Bryson, S. T., et al. 2012, ApJS, 201, 15
Hwang, K. H., Udalski, A., Shvartzvald, Y., et al. 2018, AJ, 155, 20
Ida, S., & Lin, D. N. C. 2004, ApJ, 604, 388
Johnson, S. A., Penny, M., Gaudi, B. S., et al. 2020, AJ, 160, 123
Kenyon, S. J., & Hartmann, L. 1995, ApJS, 101, 117
Koshimoto, N., Baba, J., & Bennett, D. P. 2021a, ApJ, 917, 78
Koshimoto, N., Bennett, D. P., Suzuki, D., & Bond, I. A. 2021b, ApJL, 918, L8
Koshimoto, N., & Ranc, C. 2021, nkoshimoto/genulens: A Tool for Gravitational Microlensing Events Simulation, v1.0, Zenodo, doi:10.5281/zenodo.4784949
Koshimoto, N., Udalski, A., Beaulieu, J. P., et al. 2017, AJ, 153, 1
Kroupa, P., Tout, C. A., & Gilmore, G. 1993, MNRAS, 262, 545
Lingam, M., Ginsburg, I., & Loeb, A. 2020, ApJ, 888, 102
Lissauer, J. J. 1993, ARA&A, 31, 129
Mao, S., & Paczynski, B. 1991, ApJL, 374, L37
Marcy, G., Butler, R. P., Fischer, D., et al. 2005, PThPS, 158, 24
Miyazaki, S., Johnson, S. A., Sumi, T., et al. 2021, AJ, 161, 84
Miyazaki, S., Sumi, T., Bennett, D. P., et al. 2018, AJ, 156, 136
Miyazaki, S., Sumi, T., Bennett, D. P., et al. 2020, AJ, 159, 76
Mróz, P., Udalski, A., Skowron, J., et al. 2017, Natur, 548, 183
Muraki, Y., Han, C., Bennett, D. P., et al. 2011, ApJ, 741, 22
Nataf, D. M., Gould, A., Fouqué, P., et al. 2013, ApJ, 769, 88
Nishiyama, S., Tamura, M., Hatano, H., et al. 2009, ApJ, 696, 1407
Paczynski, B. 1986, ApJ, 304, 1
Penny, M. T., Gaudi, B. S., Kerins, E., et al. 2019, ApJS, 241, 3
Poindexter, S., Afonso, C., Bennett, D. P., et al. 2005, ApJ, 633, 914
Pollack, J. B., Hubickyj, O., Bodenheimer, P., et al. 1996, Icar, 124, 62
Ranc, C., Bennett, D. P., Hirao, Y., et al. 2019, AJ, 157, 232

Rattenbury, N. J., Bond, I. A., Skuljan, J., & Yock, P. C. M. 2002, MNRAS, 335, 159
Sajadian, S., Rahvar, S., & Kazemian, F. 2021, arXiv:2103.10593
Sako, T., Sekiguchi, T., Sasaki, M., et al. 2008, ExA, 22, 51
Shin, I. G., Yee, J. C., Gould, A., et al. 2019, AJ, 158, 199
Shvartzvald, Y., Maoz, D., Udalski, A., et al. 2016, MNRAS, 457, 4089
Skowron, J., Ryu, Y. H., Hwang, K. H., et al. 2018, AcA, 68, 43
Skowron, J., Udalski, A., Gould, A., et al. 2011, ApJ, 738, 87
Sumi, T., Abe, F., Bond, I. A., et al. 2003, ApJ, 591, 204
Sumi, T., Kamiya, K., Bennett, D. P., et al. 2011, Natur, 473, 349
Suzuki, D., Bennett, D. P., Ida, S., et al. 2018, ApJL, 869, L34
Suzuki, D., Bennett, D. P., Sumi, T., et al. 2016, ApJ, 833, 145
Szymański, M. K., Udalski, A., Soszyński, I., et al. 2011, AcA, 61, 83
Terry, S. K., Bhattacharya, A., Bennett, D. P., et al. 2021, AJ, 161, 54
Udalski, A. 2003, AcA, 53, 291
Udalski, A., Szymański, M. K., & Szymański, G. 2015, AcA, 65, 1
Vandorou, A., Bennett, D. P., Beaulieu, J.-P., et al. 2020, AJ, 160, 121
Verde, L., Peiris, H. V., Spergel, D. N., et al. 2003, ApJS, 148, 195
Wozniak, P. R. 2000, AcA, 50, 421
Yee, J. C., Shvartzvald, Y., Gal-Yam, A., et al. 2012, ApJ, 755, 102
Yee, J. C., Zang, W., Udalski, A., et al. 2021, AJ, 162, 180
Yoo, J., DePoy, D. L., Gal-Yam, A., et al. 2004, ApJ, 603, 139
Zang, W., Han, C., Kondo, I., et al. 2021b, RAA, 21, 239
Zang, W., Hwang, K.-H., Udalski, A., et al. 2021a, AJ, 162, 163
Zang, W., Shvartzvald, Y., Udalski, A., et al. 2020, arXiv:2010.08732
Zhang, X., Zang, W., Udalski, A., et al. 2020, AJ, 159, 116